Naval Research Laboratory
Washington, DC 20375-5320

NRL/5604/MR—2023/1

Multi-Spectral Active IR Sensing

Jerry R. Meyer

Advanced Optoelectronics Section
Optical Sciences Division

E.M. Jackson
J.A. Nolde
E.H. Aifer

Quantum and Optical Electronics Branch
Electronics Science and Technology Division

C.S. Kim
C.L. Canedy
I. Vurgaftman

Optical Physics Branch
Optical Sciences Division

R.L. Espinola
M.R. Pauli
J.M. Auxier

Advanced Techniques Branch
Tactical Electronic Warfare Division

January 4, 2024

REPORT DOCUMENTATION PAGE

PLEASE DO NOT RETURN YOUR FORM TO THE ABOVE ORGANIZATION

1. REPORT DATE
01-04-2024

2. REPORT TYPE
NRL Memorandum Report

3. DATES COVERED
START DATE
END DATE

4. TITLE AND SUBTITLE
Multi-Spectral Active IR Sensing

5a. CONTRACT NUMBER

5b. GRANT NUMBER

5c. PROGRAM ELEMENT NUMBER

5d. PROJECT NUMBER

5e. TASK NUMBER

5f. WORK UNIT NUMBER
6C18

6. AUTHOR(S)
J. R. Meyer, E. M. Jackson, C. S. Kim, C. L. Canedy, J. A. Nolde, E. H. Aifer, R. L. Espinola, M. R. Pauli, J. M. Auxier, and I. Vurgaftman

7. PERFORMING ORGANIZATION / AFFILIATION NAME(S) AND ADDRESS(ES)
Naval Research Laboratory
4555 Overlook Ave SW
Washington, DC 20375-5320

8. PERFORMING ORGANIZATION REPORT NUMBER
NRL/5604/MR—2023/1

9. SPONSORING / MONITORING AGENCY NAME(S) AND ADDRESS(ES)
Office of Naval Research
One Liberty Center
875 N. Randolph Street, Suite 1425
Arlington, VA 22203-1995

10. SPONSOR / MONITOR'S ACRONYM(S) NUMBER
ONR

11. SPONSOR / MONITOR'S REPORT NUMBER(S)

12. DISTRIBUTION / AVAILABILITY STATEMENT

DISTRIBUTION STATEMENT A: Approved for public release; distribution is unlimited.

13. SUPPLEMENTAL NOTES

14. ABSTRACT

This program has developed resonant cavity infrared detectors (RCIDs) with very thin InAsSb/InAs superlattice absorber layers. An exemplary RCID placed an absorber with thickness only 100 nm inside a cavity formed by a GaAs/AlGaAs distributed Bragg reflector bottom mirror and Ge/SiO2/Ge top mirror. At a low bias voltage of 150 mV, the external quantum efficiency (EQE) reached 58% at the resonance wavelength 4.6 microns, with linewidth 19-27 nm. The thermal background current for a realistic system scenario with f/4 optic that views a 300 K scene was estimated by integrating the photocurrent generated by background spanning the entire mid-IR spectral band (3-5 m). The resulting specific detectivity is a factor of 3 lower than for a state-of-the-art broadband HgCdTe device at 300 K, where dark current dominates the noise. However, at 125 K where the suppression of background noise becomes critical, the estimated specific detectivity of D* of 5.5e12 cm Hz½/W is more than 3× higher. This occurs despite a non-optimal absorber cut-off that causes the EQE to decrease rapidly with decreasing temperature, e.g., to 33% at 125 K. The RCID's advantage over the broadband device depends critically on its low EQE at non-resonance wavelengths, which was ≤ 1% in the range 3.9-5.5 microns. Simulations using NRL MULTIBANDS found that at ambient temperature, the primary source of dark current is impact ionization in the top contact layer. This can be mitigated in future work by reducing the doping concentration in the top contact layer. We expect the planned design modifications to substantially enhance D* at all temperatures from cryogenic to ambient. Another RCID advantage is high frequency response, because photoexcited carriers can be extracted rapidly from the very thin absorber. Collaborator Intraband, LLC performed high-frequency measurements on an RCID grown by NRL and processed by Praevium to have a smaller mesa diameter of 25 microns for low capacitance. At T = 20 °C and 5 Gb/s data rate, the device with EQE = 52% at the resonance peak was found to have a bit-error-ratio (BER) < 10e-7. The -3 dB frequency response at 1 V bias was 7 GHz. Although high peak EQE is observed at lower bias, the RCIDs tested to date have required a higher voltage to sweep photoexcited carriers out of the absorber rapidly enough for high frequency response.

15. SUBJECT TERMS

16. SECURITY CLASSIFICATION OF:

a. REPORT	**b. ABSTRACT**	**c. THIS PAGE**	**17. LIMITATION OF ABSTRACT**	**18. NUMBER OF PAGES**
U	U	U	SAR	28

19a. NAME OF RESPONSIBLE PERSON
Jerry R. Meyer

19b. PHONE NUMBER *(Include area code)*
(202) 767-3276

This page intentionally left blank.

Multi-Spectral Active IR Sensing

Summary:

Under this program, we developed resonant cavity infrared detectors (RCIDs) with very thin InAsSb/InAs superlattice absorber layers. An exemplary RCID placed an absorber with thickness only ≈ 100 nm inside a cavity formed by a 33-period GaAs/$Al_{0.92}Ga_{0.08}As$ distributed Bragg reflector bottom mirror and Ge/SiO_2/Ge top mirror. At a low bias voltage of 150 mV, the external quantum efficiency (EQE) for a device with 93 μm mesa diameter reached 58% at the resonance wavelength $\lambda_{res} \approx 4.6$ μm, with linewidth $\delta\lambda$ = 19-27 nm. The thermal background current for a realistic system scenario with f/4 optic that views a 300 K scene was estimated by integrating the photocurrent generated by background spanning the entire mid-IR spectral band (3-5 μm). The resulting specific detectivity is a factor of 3 lower than for a state-of-the-art broadband HgCdTe device at 300 K, where dark current dominates the noise. However, at 125 K where the suppression of background noise becomes critical, the estimated specific detectivity of D^* of 5.5×10^{12} cm Hz^{½}/W is more than 3× higher. This occurs despite a non-optimal absorber cut-off that causes the EQE to decrease rapidly with decreasing temperature, *e.g.*, to 33% at 125 K. The RCID's advantage over the broadband device depends critically on its low EQE at non-resonance wavelengths, which was ≤ 1% in the range 3.9-5.5 μm. Simulations using NRL MULTIBANDS^{TM} found that at ambient temperature, the primary source of dark current is impact ionization in the top contact layer. This can be mitigated in future work by reducing the doping concentration in the top contact layer. We expect the planned design modifications to substantially enhance D^* at all temperatures from cryogenic to ambient.

Another RCID advantage is high frequency response, because photoexcited carriers can be extracted rapidly from the very thin absorber. Collaborator Intraband, LLC performed high-frequency measurements on an RCID grown by NRL and processed by Praevium to have a smaller mesa diameter of 25 μm for low capacitance. At T = 20 °C and 5 Gb/s data rate, the device with EQE = 52% at the resonance peak was found to have a bit-error-ratio (BER) < 10^{-7}. The -3 dB frequency response at 1 V bias was 7 GHz. Although high peak EQE is observed at lower bias, the RCIDs tested to date have required a higher voltage to sweep photoexcited carriers out of the absorber rapidly enough for high frequency response.

Manuscript approved December 14, 2023.

A. Objective:

To develop a new generation of resonant cavity infrared detectors (RCIDs) that display dramatically higher sensitivity to a narrow spectral bandwidth, such as that emitted by an IR laser, than any broadband IR detector now available.

B. Motivation:

The Navy requirements for advanced MWIR and LWIR detectors fall into two broad application classes. The first is thermal imaging by a focal plane array (FPA), to provide high-resolution vision and identification in near or total darkness. This requires a broad spectral bandwidth to maximize the net signal within a given atmospheric window such as 3-5 or 8-12 μm. Maximizing the sensitivity to reach background-limited performance (BLIP) generally requires cryogenics.

The second broad application class requires high sensitivity only within a narrow spectral band. This occurs when the signal to be detected is produced by an IR laser with known fixed wavelength. Examples include optics detection, beacon detection, UAV detection/classification, active imaging, target designation, sensing in degraded visual environments, covert free-space communications, laser spectroscopy for chemical/biological/explosives sensing, and hyperspectral imaging. Although hyperspectral imaging can be realized by mechanically placing a series of narrow spectral filters in front of a broadband FPA, that approach is cumbersome and reduces rather than enhances the detection sensitivity within each narrow spectral band owing to the transmission loss.

Even though these two application classes have very different requirements (broadband detection, *vs*. high sensitivity within a narrow spectral bandwidth), fielded Navy systems use broadband detectors (such as those used in thermal imaging) for both because devices tailored to the second set of requirements do not exist at present. RCIDs can for the first time provide practical enhancement of the sensitivity and/or operating temperature within a narrow IR spectral bandwidth, and also offer much faster frequency response. At the same time, optical background clutter at wavelengths outside the narrow bandwidth of interest is greatly reduced. This will allow both laser detectors and multi-spectral imagers to display background-limited performance at higher operating temperatures than is currently possible, for substantial reduction of the size, weight, and power (SWaP).

C. Background:

Interband detectors operating in the midwave infrared (MWIR, defined here as λ = 3-5 μm) generate photocurrent when incident light is absorbed in a layer with bandgap smaller than the photon energy. For a conventional photovoltaic architecture that provides at most two passes through the device following possible reflection from a metallized contact, the absorber must be several microns thick to produce high external quantum efficiency (EQE). However, a resonant cavity infrared detector (RCID) can maintain high EQE in a narrow spectral bandwidth even when the absorber is very thin, by imposing multiple passes between top and bottom mirrors [1]. This can be advantageous if the light to be detected is from a laser rather than broadband thermal radiation, or when limited bandwidth is desired as in chemical sensing spectroscopy or hyperspectral imaging. To minimize noise currents associated with the broadband background, the RCID should not only have a narrow spectral bandwidth, but must also minimize the detection of wavelengths outside the narrow band of interest. The RCID architecture also provides enhanced frequency response, since photogenerated carriers can be collected more rapidly from a thin absorber.

The RCID concept has been developed extensively at shorter wavelengths [2,3], where resonant cavity photodiodes with enhanced frequency response are relatively mature. However, until recently no MWIR RCIDs had combined low dark current with high peak quantum efficiency. In 2003, a group at Imperial College reported an RCID with InAs absorber grown on a 10-period GaAs/AlGaAs distributed Bragg reflector (DBR) [4]. The cavity was completed by a CrAu top mirror that also provided electrical contact. The photocurrent was highest at $T = 205$ K, where $\lambda_{res} \approx 3.3$ μm and the full-width at half maximum (FWHM) of the spectral bandwidth ($\delta\lambda$) was ≈ 150 nm under 3 V bias. No dark current (J_{dark}) or specific detectivity (D^*) was reported. In the period 2004-2012, groups at U. Linz. [5], ETH Zurich [6], and MIT [7] reported the incorporation of various lead-salt absorbers into RCID cavities defined by combining grown lead-salt bottom mirrors with metal [5,6] or lead-salt top mirrors [7]. Peak wavelengths ranged from 3.45 μm to 8.4 μm, with resonance linewidths typically 36-90 nm. ETH Zurich tuned the resonance wavelength by shifting the position of an external top metal mirror, either piezoelectrically [8] or with a microelectromechanical system (MEMS) [9]. EQEs up to 90% were reported for the lead-salt RCIDs, although accompanied by relatively low resistance-area products (R_0A). Consequently, D^* was always at least 2 orders of magnitude lower than the Rule '07 value [10] for a state-of-the-art (as of 2007) broadband HgCdTe photodiode with cut-off equal to the resonance wavelength (λ_{res}) at the same operating temperature.

In 2017, U. Rochester and Amethyst Research reported an RCID with 100-nm-thick bulk InAs absorber surrounded by grown top and bottom GaAsSb/AlAsSb DBRs [11]. The resonance wavelength was $\lambda_{res} = 2.91$ μm, with spectral linewidth $\delta\lambda \approx 45$ nm. Although the dark current density of 0.4 mA/cm^2 at 298 K was slightly below Rule '07, no EQE or D^* was reported.

Two years later, NRL reported the first RCID to exhibit high performance at a mid-IR wavelength beyond 3 μm [12]. At $\lambda_{res} = 4.0$ μm, the device with grown GaSb/AlAsSb bottom DBR, silver top mirror, and absorber thickness only 50 nm attained external quantum efficiency EQE = 34%, with linewidth $\delta\lambda = 46$ nm and $D^* = 7 \times 10^9$ cm Hz^{½}/W at room temperature. If we define $\Gamma_{D^*} = D^*_{RCID}/D^*_{Rule07}$, where the denominator is obtained by combining Rule '07 dark current with EQE = 85%, the value for this device was $\Gamma_{D^*} \approx 0.18$. Also in 2019, a team led by U. Lancaster reported an RCID with 96-nm-thick InAsSb absorber that displayed 62% EQE at 300 K for $\lambda_{res} \approx 3.7$ μm and $\delta\lambda = 42$ nm [13]. At 250 K, the detectivity $D^* = 8 \times 10^{10}$ cm Hz^{½}/W yields $\Gamma_{D^*} \approx 0.4$. U. Lancaster also reported an RCID with InAs-InAsSb superlattice absorber that operated with $\lambda_{res} \approx 4.4$ μm, $\delta\lambda = 50$ nm, 80% EQE, and $D^* = 2.5 \times 10^{10}$ cm Hz^{½}/W at 240 K ($\Gamma_{D^*} \approx 0.2$) [14]. The same group demonstrated RCIDs with $\lambda_{res} \approx 7.7$ μm, although at 77-140 K the Γ_{D^*} values were < 0.01 [15]. In 2021, they reported an RCID with bulk InAsSb absorber, $\lambda_{res} \approx 3.7$ μm, and $\delta\lambda \approx 40$ nm that attained $\Gamma_{D^*} \approx 0.4$-0.5 at temperatures from 200 to 300 K [16]. They also reported non-dynamic wavelength tuning, from $\lambda_{res} \approx 1.98$ to 2.08 μm, by fabricating a series of cavity thicknesses on the same chip [17].

University of Texas recently employed an alternative approach to forming the resonant cavity, in which a high-contrast grating etched into the top of the semiconductor epilayer couples IR input into in-plane waveguide modes [18]. Light is confined to the waveguide by a heavily-doped semiconductor layer grown below the absorber. Devices with $\lambda_{\mathrm{res}} \approx 4.4$ μm and 4.7 μm yielded up to 60% EQE with ≈ 60 nm linewidth. The detectivity was as high as $\Gamma_{D^*} \approx 0.5$ at room temperature, although riding on a large non-resonant background and for only one polarization of the incoming light relative to the grating orientation. An LWIR RCID with $\lambda_{\mathrm{res}} \approx 10.8$ μm was also demonstrated [19].

Apart from the U. Texas devices that did not employ DBRs, all of the MWIR RCIDs discussed above employed bottom DBRs and absorbers that were grown or deposited as a single structure. For the higher-performance RCIDs grown by III-V molecular beam epitaxy (MBE) on GaSb or InAs substrates [11-17], this requires the challenging growth of thick GaSb/AlAsSb or GaAsSb/AlAsSb DBRs while maintaining precise control over each layer thickness. The roughly linear scaling with wavelength requires a bottom mirror thickness of 14 μm for the device with $\lambda_{\mathrm{res}} \approx 7.7$ μm [15].

D. Technical Approach:

NRL has established leadership in the design, growth and processing of III-V semiconductor detectors for MWIR and LWIR imaging. In particular, we have reported multiple advances in the state of the art for devices employing type-II superlattice (SL) materials such as InAs/Ga(In)Sb and InAs/InAsSb.

Assuming that surface leakage and generation-recombination currents (associated with internal voltages) can be suppressed, the fundamental mechanism limiting the minimum detectable optical signal is the diffusion contribution to the dark current. Since this is created by thermal generation within the absorber, its magnitude scales with the absorber thickness. For this reason, the RCID's ultra-thin absorber can potentially reduce the diffusion dark current density by two orders of magnitude, which translates into an order-of-magnitude reduction of the primary noise source.

E. Progress:

In FY21, Code 5700 assembled a suitable test dewar, and using preliminary RCIDs qualified the apparatus for testing in a specific EW mission scenario. Code 5600 used the custom software package NRL MULTIBANDS$^{\mathrm{TM}}$ to simulate RCID performance, and found that the most promising architecture is likely to be a barrier structure (*nBn*) rather than a *p-n* junction. Ga-free *nBn* structures with thin InAsSb/InAs superlattice absorbers were grown by molecular beam epitaxy (MBE) and processed into devices. Time-dependent photoluminescence experiments performed by Code 6800 confirmed free carrier lifetimes ≥ 1 μs in the superlattice absorbers at 150-250 K. At room temperature the lifetime was ≈ 300 ns, a substantial improvement over the lifetimes of only 10-50 ns in the first NRL RCIDs structures from 2019 [12].

In FY22, Code 5700 implemented a laboratory test setup to evaluate and compare the RCID performance against a conventional broadband detector for an application involving the optical signatures of notional circular apertures. Beam expansion and focusing optical components were also procured to support characterization of the external quantum efficiency (EQE). Code 5600 used MBE to grow 22 different nBn detector designs with cut-off wavelength ≈ 4.6 μm, absorber thicknesses ranging from 50 nm to 1 μm, and various doping levels of the absorber and barrier. Material from each wafer was processed into test devices without top and bottom mirrors, and then characterized to determine the performance characteristics. The dark current and spectral dependence of the external quantum efficiency (EQE) were measured as a function of temperature between 150 K and 300 K. A substantial improvement was observed when the order of the layering was flipped, such that the absorber was grown above the barrier layer rather than below as in all of the earlier structures. This modification decreased the dark current at 200 K by nearly a full order of magnitude. The dramatic improvement appears due to reduction of a strong internal electric field that had been induced by the large conduction band offset between the bottom contact layer (same composition as the InAs-InAsSb absorber) and the GaSb buffer layer. Many of the other investigated design modifications had less influence on the device performance.

In FY23, Code 5700 used an RCID with high EQE at the resonance peak to perform optics detection experiments in the laboratory. Sensitivity with the RCID was compared to that for a broadband FLIR A6750 Cooled MWIR camera (which incorporates a strained type-II superlattice absorber). However, the comparisons at 300 K and 77 K were not definitive because the emission wavelength of the available QCL (≈ 4.62 μm) was too long for overlap with the RCID resonance peak at lower temperatures where the RCID should be advantageous. New RCID devices were fabricated with considerable simplification of the GaSb-based growth, because rather than employing a grown GaSb/AlAsSb Bragg mirror for reflection on the bottom of the cavity, the detector wafer with thin *nBn* absorber was heterogeneously bonded to a commercially-purchased GaAs/$Al_{0.92}Ga_{0.08}As$ DBR with reflectivity > 99%. The bonding was performed by collaborators at Praevium Research. This approach combines a higher cavity quality factor (*Q*) with higher growth and processing yield. For high frequency response, a further advantage is much lower capacitance of the semi-insulating GaAs compared to GaSb or InAs, for which no semi-insulating substrates are available. As will be discussed in the following Sections, detector materials with absorbers only 100 nm thick and the most favorable design were provided to Praevium for heterogeneous bonding to the GaAs/AlGaAs bottom mirror, followed by deposition of a single-period dielectric top mirror to complete the RCID cavity.

E.1 Design, MBE growth, and material characterization

The *nBn* detector structure was grown on a 2" heavily-*n*-doped GaSb substrate in a Riber Compact 21T molecular beam epitaxy (MBE) system [20]. To begin, the native oxide layer was removed *in situ* by heating the substrate slowly under cracked antimony flux to 550 °C and dwelling for 15 minutes. This was followed by cool down to 495 °C, where a 500-nm-thick GaSb buffer layer was grown at 1 ML/s. Next the wafer was cooled to 450 °C and a lattice-matched $InAs_{0.91}Sb_{0.09}$ etch stop layer and *n*-type GaSb sacrificial layer were grown. These layers aided the eventual removal of the GaSb substrate after bonding to the GaAs/$Al_{0.92}Ga_{0.08}As$ bottom DBR. The *nBn* detector structure, which was also grown at ~ 450 °C, consisted of a 300-nm-thick *n*-type InAs/$InAs_{0.6}Sb_{0.4}$ superlattice top contact layer, 200-nm-thick unintentionally-doped InAs/AlSb superlattice barrier layer, unintentionally-doped InAs/$InAs_{0.6}Sb_{0.4}$ superlattice absorber layer with 20 periods and total thickness 103 nm, 250-

nm-thick *n*-type InAs/$InAs_{0.6}Sb_{0.4}$ superlattice bottom contact layer, and 20-nm-thick n^+-InAs bottom contact capping layer (see the band diagram in Fig. 14 below). Prior to growth of the device wafer, high-resolution x-ray diffraction and photoluminescence (PL) measurements were performed on separately-grown samples with thicker (≈ 0.5 μm) absorbers, in order to calibrate the lattice matching, measure the carrier lifetime, calibrate the detector cut-off wavelength, and assess the surface morphology. Figure 1 shows the high-resolution θ-2θ x-ray scan for the wafer from which the devices were processed.

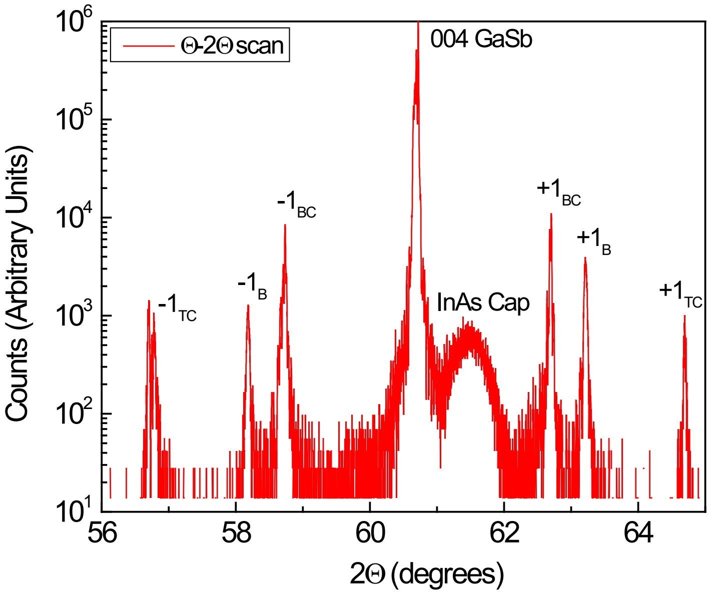

Fig. 1: High resolution θ-2θ x-ray diffraction scan for the wafer from which the devices were processed (BC = bottom contact layer / absorber layers, B = barrier layer, TC = top contact layer).

The minority-carrier lifetime in a PL structure with similar absorber superlattice was determined *vs.* photoexcited carrier concentration by measuring the optical response roll-off as a function of the modulation frequency of a 1064 nm pump laser. Figure 2 shows that the recombination lifetime at low injected concentrations was ≈ 300 ns at 300 K and 0.7-1 μs at 150-250 K. This contrasts a much shorter lifetime of ≈ 50 ns in the Ga-containing "W" structure grown for NRL's earlier RCID demonstration [12].

To evaluate the underlying *nBn* detector performance, devices without top and bottom mirrors were first processed from the same wafer material. Optical lithography with a two-step wet etch [21] was used to fabricate circular mesas using processing that was described previously [12]. At the RCID operating biases of -150 mV, a device with mesa diameter 200 μm had dark current densities of 0.29 A/cm^2 at 300 K, 0.012 A/cm^2 at 250 K, 1.7×10^{-4} A/cm^2 at 200 K, and 6.1×10^{-7} A/cm^2 at 150 K.

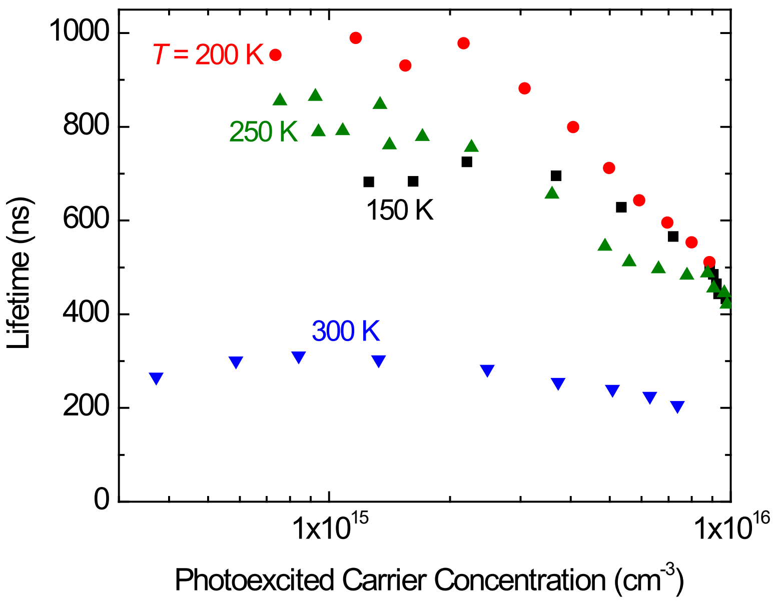

Fig. 2: Lifetime *vs.* photoexcited carrier concentration at a series of temperatures in a PL structure with similar absorber superlattice, as determined by measuring the optical response roll-off as a function of the modulation frequency of a 1064 nm pump laser.

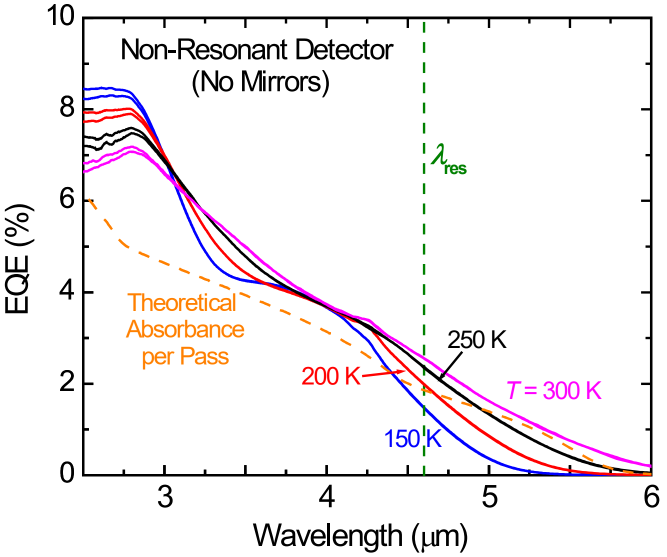

Fig. 3: External quantum efficiency spectra at a series of temperatures for a non-resonant detector processed from the same wafer material as the RCID. The dashed orange curve shows the theoretical absorbance per pass at 300 K from an 8-band ***k·p*** calculation.

Figure 3 shows EQE spectra at a series of temperatures for one of these detectors. The spectrum at 300 K indicates a cut-off wavelength only slightly longer than the target of ≈ 5.1 μm. This EQE was obtained for a mesa with fully-metallized top contact and illumination through the *n*-doped GaSb substrate, which was not anti-reflection coated. While a full comparison of the theoretical and experimental absorption spectra would require an accurate characterization of the metal reflectivity and substrate absorption, the shape and magnitude of the theoretical absorbance per pass at 300 K from an 8-band $\boldsymbol{k}\cdot\boldsymbol{p}$ calculation (dashed orange curve) is similar to those of the measured EQE.

E.2 RCID fabrication

To process RCID devices, an 11 mm × 11 mm chip from the *nBn* detector wafer was bonded to a commercially-purchased GaAs/$Al_{0.92}Ga_{0.08}As$ mirror that was grown on a semi-insulating GaAs substrate. A total of 33 DBR periods was obtained by bonding two mirror segments together, which provided > 99% reflectance in the 4.4-4.7 μm spectral band. Bonding of the GaSb-based chip began with deposition of a 100Å-thick interfacial dielectric layer at the bond interface, followed by plasma activation and low-temperature bonding below 250 °C. After bonding, the GaSb substrate was removed by a chromic-acid-based etch that stopped on the InAsSb etch stop layer. The etch stop and sacrificial GaSb layers were then removed by chemical etching before the detectors were fabricated by lithographic processing.

The first step in fabricating the reticulated shallow etched mesa isolation (RSEMI) detector structures [21] was to define an alignment layer. Then the top ring contact metallization was deposited, followed by a shallow mesa etch that stopped just below the top contact layer. Next a second deep etch proceeded to the bottom contact layer, followed by deposition by plasma enhanced chemical vapor deposition (PECVD) of an SiO_2 passivation layer on the sidewalls. A further etch proceeded through the bottom contact, stopping at the top of the semi-insulating GaAs/$Al_{0.92}Ga_{0.08}As$ mirror. This was followed by another SiO_2 deposition. Top and bottom contact openings were defined through the SiO_2, followed by the deposition of Ti/Pt/Au contact metal and ground signal ground (GSG) pads to enable high speed operation. Devices with active diameters ranging from 15 to 100 μm were fabricated in a single run.

To shift the cavity length and λ_{res}, Ge spacers of varying thickness were deposited on top of the *nBn* detector structure. Then quarter-wave SiO_2 and Ge layers were deposited to complete the Ge/SiO_2/Ge top mirror. Figure 4 schematically illustrates side and top views of the full structure for a single device.

The planned Ge thicknesses of 148, 153, and 158 nm were intended to tune the resonance wavelength from 4.60 to 4.62 μm. However, unexpected variation of the deposition thickness led to a much greater shift of λ_{res}. The results below were obtained for a device with mesa diameter 93 μm and nominal Ge thickness 158 nm, for which the resonance wavelength was close to the projected value of 4.62 μm. However, the devices with 148 and 153 nm spacer thicknesses had shorter-than-expected resonance wavelengths of 4.56 and 4.59 μm, respectively. The maximum EQE also decreased with decreasing spacer thickness, probably due to higher absorption loss in the bottom superlattice contact layer at shorter wavelengths.

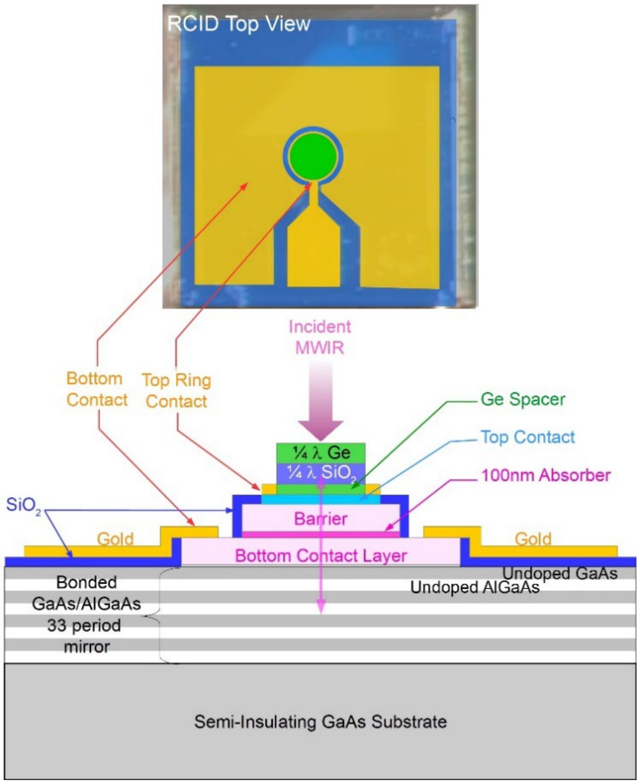

Fig. 4: Schematic of the RCID layer structure and patterned device geometry, from the side (lower) and top (upper).

E.3 Experimental results – *J-V* characteristics

The device was mounted on a 68-pin LCC and loaded into a liquid nitrogen flow dewar with an internal cold shield held at $T \approx 78$ K. The dark *J-V* characteristics at temperatures between 100 K and 300 K were taken with an HP4145A parameter analyzer.

Figure 5 shows the dark current density (J_d) *vs.* voltage at a series of temperatures for the RCID device with absorber thickness 103 nm, mesa diameter 93 µm, and Ge spacer thickness 158 nm. The vertical dashed line indicates the bias voltage V_b = -150 mV at which the EQE dependence on voltage is nearly saturated. At that voltage, the dark current densities are 1.3-3× higher than for the detectors processed without mirrors.

Figure 6 plots the dark current density, scaled by $T^{-2.5}$, *vs.* inverse temperature for the RCID operating at V_b = -150 mV. The temperature scaling accounts for the carrier densities of states that are approximately 3D for electrons and 2D for holes. The data fit a single slope (dashed line) over the entire temperature range from 125 to 300 K. The corresponding activation energy of ≈ 217 meV is a little smaller than the nominal bandgap of ≈ 250-275 meV deduced from the EQE spectra in Figure 3. Figure 5 plots the resistance-area product ($RA = dV/dJ$) *vs.* inverse temperature at the operating bias, which will enter into the evaluation of D^* in Eq. (1) below. All of the devices with different Ge spacer layer thicknesses displayed similar *J-V* characteristics.

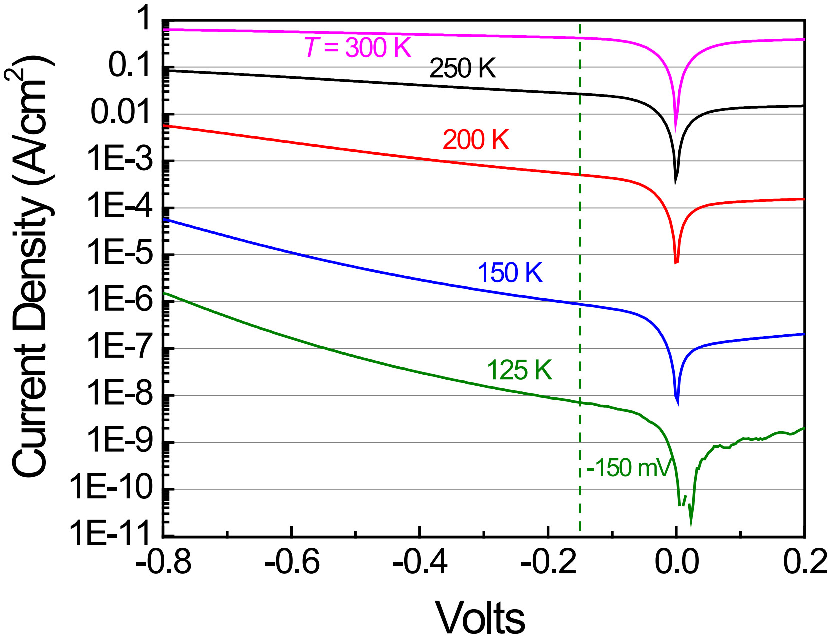

Figure 5 - Dark current density *vs.* voltage at a series of temperatures for the present RCID device with absorber thickness 103 nm, mesa diameter 93 µm, and top Ge spacer thickness 158 nm. The vertical dashed line represents the bias voltage of -150 mV employed in the detection experiments.

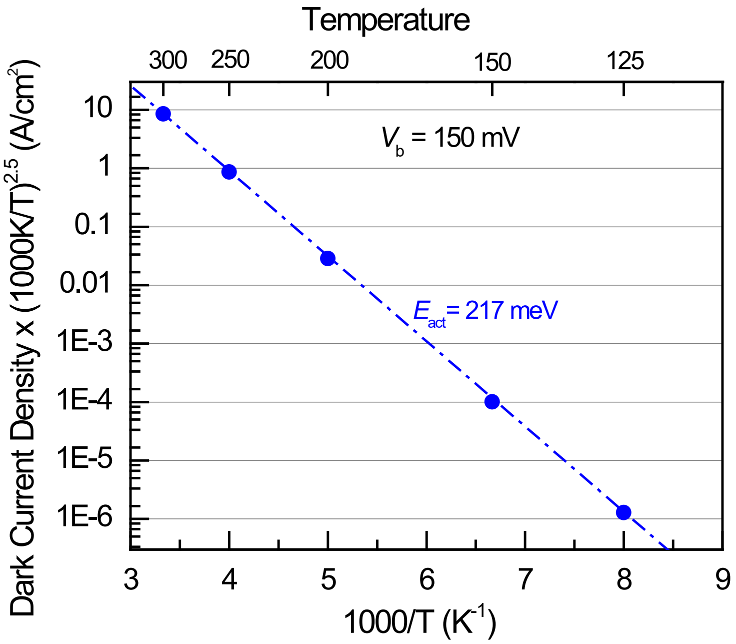

Figure 6 - Dark current density scaled by $T^{-2.5}$ *vs.* inverse temperature for the RCID operating at a fixed reverse bias of -150 mV. The fit to a linear dependence indicates an activation energy of ≈ 217 meV.

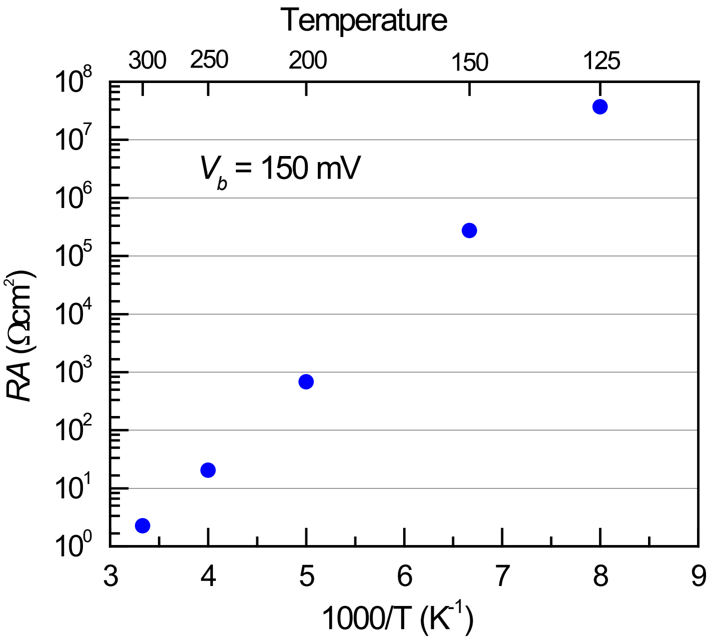

Figure 7 – *RA* for the RCID *vs.* inverse temperature.

E.4 Experimental results – External quantum efficiency and *D**

The blue curve in Fig. 8 illustrates the transmissivity spectrum of the *nBn* detector chip bonded to the GaAs/$Al_{0.92}Ga_{0.08}As$ bottom DBR, following removal of the GaSb substrate but before deposition of the top mirror. As expected, the transmission is negligible within the region λ = 4.4-4.7 μm where the DBR's reflectivity exceeds 99%. The reflectivity of the fully-processed RCID is given by the red curve. The sharp minimum at λ = 4.618 μm coincides with the cavity resonance, as will be seen below.

Optical measurements were taken in the same dewar as the *J-V* characterization, but with an aperture replacing a blank in the cold shield. The responsivity spectrum was measured with an IS50 Fourier Transform IR (FTIR) spectrometer. The IR source beam was focused to a diameter of ≈ 80 μm centered on the RCID mesa, and the RCID's photocurrent fed back into the FTIR to obtain a raw spectrum. The source spectrum was then measured at the position of the RCID with a DTGS detector corrected for its frequency response. The RCID responsivity $R(\lambda)$ is proportional to the raw spectrum divided by the source spectrum, and the EQE spectrum is proportional to $R(\lambda)/\lambda$.

In order to normalize the EQE spectrum, the absolute EQE at resonance was measured using a black body source at 1300 K, with a filter centered near the RCID resonance frequency. The black body output was chopped at 37 Hz, and the photocurrent determined with a lock-in amplifier. The optical power incident at the RCID position was measured with a calibrated pyroelectric detector. The beam was focused to underfill the RCID mesa, and the beam diameter was varied in the range ≈ 15-64 μm. The detector response was determined from the slope of the photocurrent *vs.* area, and the absolute EQE finally calculated from the detector response and previously-determined spectrum.

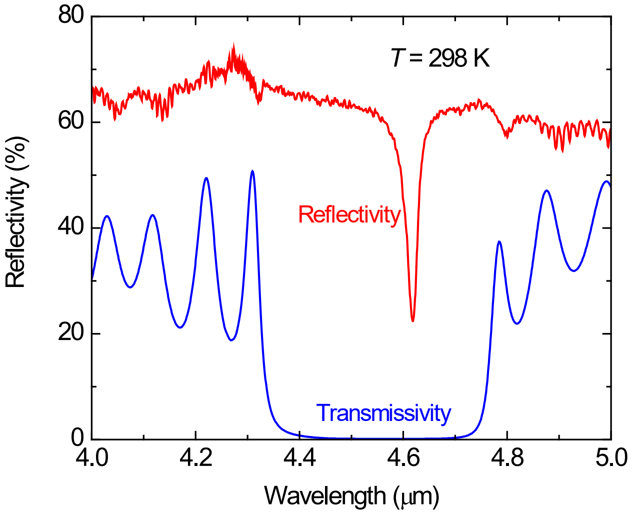

Figure 8 – Transmissivity spectrum of the *nBn* detector chip bonded to the GaAs/$Al_{0.92}Ga_{0.08}As$ DBR, following removal of the GaSb substrate but before deposition of the top mirror (blue curve), and reflectivity spectrum of the fully-processed RCID (red curve).

Figure 9 illustrates the resulting EQE spectra for the RCID at T = 125 K (green) and 300 K (magenta), for wavelengths spanning the entire MWIR spectral band. The inset shows the same data on a semi-log scale, to emphasize that the EQE remains quite small at off-resonance wavelengths spanning 3.8 μm < λ < 5.5 μm.

The magenta curve in Fig. 10 expands the EQE spectrum at 300 K near the resonance wavelength of 4.618 μm. The FWHM linewidth of 27 nm agrees well with the simulated value 26 nm, although the peak EQE of 58% is a little smaller than the theoretical projection of ≈ 70%.

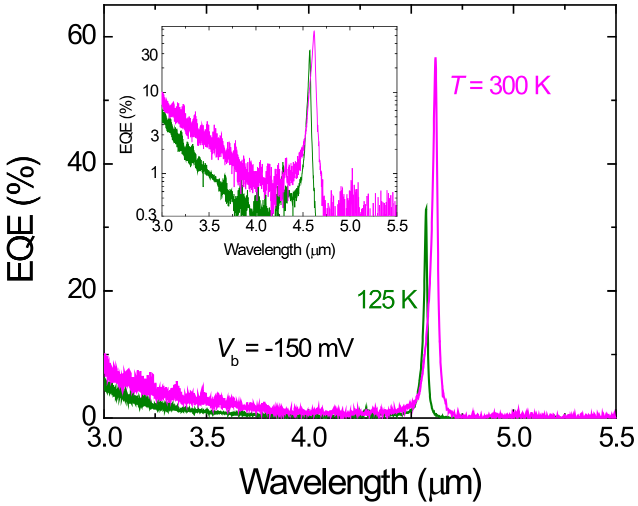

Figure 9 – External quantum efficiency at T = 125 K (green) and 300 K (magenta), as measured with the FTIR over a broad spectral band. The insert shows the same data on a semi-log scale. For wavelengths near resonance, the detector responsivity is ≈ 3.7 × EQE, which corresponds to a peak value of ≈ 2 A/W at 300 K.

The EQE spectrum for the same device was also quantified over a limited range of wavelengths by measurements by both Code 5700 and our Intraband, LLC. Both measured the photocurrents induced by quantum cascade lasers (QCLs) with known incident powers. The experiment by Code 5700 employed a focused QCL with center wavelength 4.7 μm and beam size 2.3 × 3.5 mm. At a drive current of 1 A, temperature tuning produced three discrete wavelengths of 4.613 (15 °C), 4.628 (18 °C), and 4.641 μm (21 °C). The beam with nominal power < 10 mW passed first through a Lasnix metal grid step attenuator (ND filter), and then through an Andover bandpass filter with bandwidth 150 nm centered on 4.58 μm. A 55/45 beam splitter diverted part of the beam to a power meter, which provided *in-situ* monitoring of any optical feedback effects on the QCL. Transmission through the beam splitter next passed through optics that expanded the beam by 3× and then focused it to a nominal spot size of < 100 μm, which was small enough to underfill the RCID diameter. The RCID chip was placed in a Senseeker dewar test unit (DTU) with silicon window, although the dewar was operated at 300 K for all the measurements. The RCID signal observed under -150 mV bias was sent through a current preamplifier and lock-in amplifier modulated at 200 Hz. The results, shown as the magenta points in Fig. 10, are nominally consistent with those obtained from the FTIR characterization.

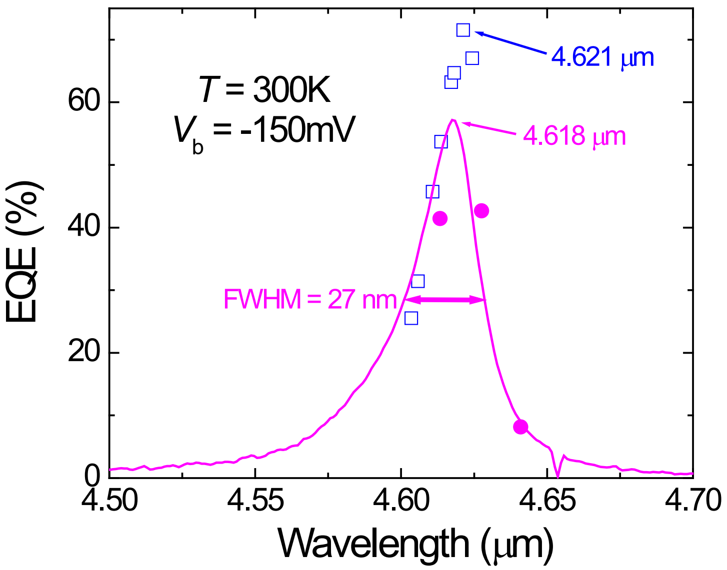

Figure 10 – EQE at 300 K over a much narrower spectral bandwidth near the resonance wavelength, as measured by three different experiments. The magenta curve was obtained by the FTIR as in Fig. 9, whereas the points were derived from measurements of the photocurrent excited by a quantum cascade laser with calibrated intensity by Code 5700 (magenta) and Intraband (blue).

The experiment at Intraband employed a single-mode distributed feedback (DFB) QCL fabricated at U. Wisconsin - Madison [22]. Its wavelength could be varied from 4.6035 to 4.6244 μm through a combination of current and temperature tuning. An uncoated glass slide with strong absorption in the MWIR attenuated the laser power from its nominal output of 20 mW to ≈ 400 μW. This was monitored via reflection from the glass slide to a power meter. An MWIR-coated beam splitter directed half of the power to an FTIR for wavelength monitoring. A CaF_2 lens with estimated transmission 99% and focal length 40 mm collimated the beam for coupling to the RCID. Any optical feedback effect on the QCL output could be monitored by the *in-situ* power and wavelength measurements. None were observed in this case, likely due to the strong attenuation by the glass slide. The input signal was incident through the 88-μm-diameter opening of the RCID's top annular contact. The EQE at each wavelength was determined by subtracting the dark current of ≈ 50 μA from the photocurrent measured at -800 mV operating bias, and then dividing by the photon density corresponding to the calibrated excitation power. The resulting EQEs are shown as the blue points in Fig. 10. The slightly-longer peak wavelength (4.621 μm) compared to that from the FTIR characterization (4.618 μm) may be due to uncertainty in the temperature calibrations of the two experiments. The peak EQE of 71%, as compared to 58% from the FTIR experiment, may be attributed in part to the use of a larger bias voltage of -800 mV, as compared to -150 mV in both experiments performed by Code 5700. At 250 K, the photocurrent measured by Code 5700 was 7% higher at -800 mV than at -150 mV. Other potential sources of discrepancy include interference with scattered light in the FTIR experiment (the probable source of the oscillations at shorter wavelengths in Fig. 9), and accumulated small errors that could total ±10% in the QCL experiment. The largest uncertainty in the simulation is parasitic absorption in the superlattice top contact and dielectric top mirror layers.

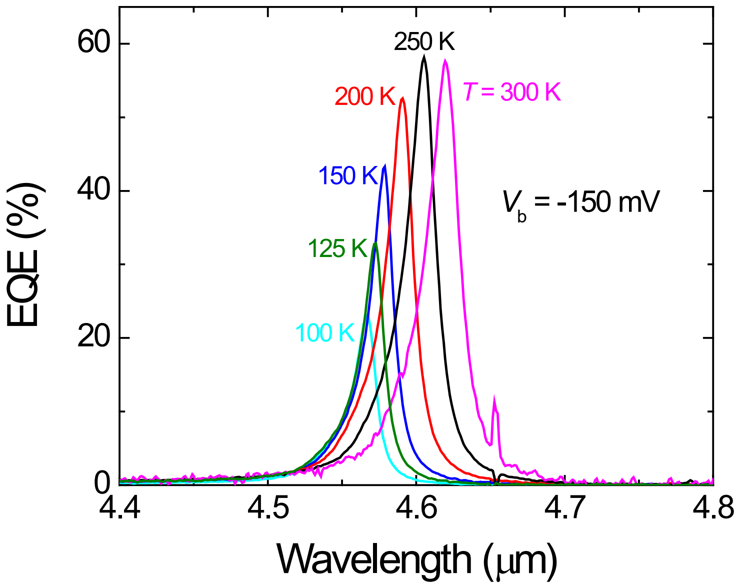

Figure 11 – EQE spectra near resonance, as determined by the FTIR characterization at a series of temperatures between 100 K and 300 K. All measurements were performed at a fixed bias voltage of -150 mV.

Figure 11 illustrates the EQE spectra near resonance at a series of temperatures in the range 100-300 K, as measured by the FTIR experiment. The resonance wavelength is seen to decrease gradually with temperature, as expected due to the decreasing refractive index of the III-V semiconductor materials in the cavity. Also apparent is a substantial decrease of the maximum EQE with decreasing temperature below 200 K. This may be due primarily to weaker absorption in the active quantum wells as the cut-off wavelength becomes shorter than λ_{res} (see Fig. 3). In future designs, this can be addressed by either a longer cut-off/shorter resonance wavelength (to increase the low-temperature absorption at the cavity resonance) or else by a higher cavity Q (more passes through the absorber induced by a more reflective top mirror, to compensate for weaker absorption per pass). The lower EQE naturally reduces the maximum D^* that is attainable at low T.

The specific detectivity may be determined from the expression:

$$D^* = \frac{q}{hc} \cdot \frac{\lambda \cdot EQE}{\sqrt{2(qJ_d + qJ_b + 2kT/RA)}} \tag{1}$$

where J_d is the dark current density at the bias voltage V_b, J_b is the photocurrent density generated by the thermal background at wavelengths both within and outside the narrow resonance bandwidth, and $2k_BT/RA$ relates to thermal carrier noise. For the present device, this contribution is non-negligible but never dominant. It is roughly 5% of the dark current contribution at 300 K, and closer to 10% at lower temperatures. Previous reports of D^* for resonant-cavity IR detectors have accounted only for the first, or at most the first and third, of the three relevant noise contributions in the denominator of Eq. (1).

A primary advantage of the RCID approach is its potential to strongly suppress thermal background noise at wavelengths outside the narrow spectral resonance. However, this advantage is only realized when EQE outside the resonance bandwidth remains quite small. Otherwise, background photocurrent can still easily dominate the net noise current. To illustrate, we consider the present RCID's potential to suppress background noise in a realistic scenario.

For a given background temperature, T, the differential power per unit area and solid angle, $L_{\text{int}}(\lambda, T)$, received by the RCID within a given differential wavelength band is [23]:

$$L_{int}(\lambda, T) = \left\{ \frac{2hc^2}{\lambda^5 \left[\exp\left({hc}/{\lambda kT} \right) - 1 \right]} \right\} /sr \approx \left(\frac{2hc^2}{\lambda^5} \right) \exp\left({-hc}/{\lambda kT} \right) /sr. \tag{2}$$

since $hc \gg \lambda k_B T$ under all conditions of interest. We will consider a scene temperature T_b that may be distinct from the detector operating temperature T_D. Division by $\hbar\omega$ gives the differential incident photon flux density, and to integrate over all incident angles we multiply by π. However, if an input optic restricts the detector field of view that observes the external scene, we should also multiply by the external background at temperature T_b by the fraction F that observes it, while the remaining fraction (1-F) observes background at the cold-shield temperature T_D. The differential photocurrent density generated by the background flux is also proportional to the detector's EQE(λ, T_D) at the given wavelength. The total background flux is then:

$$L_J(\lambda, T_b, T_D) = \left(\frac{\pi q}{\hbar\omega} \right) \times EQE(\lambda, T_D) \times \left[F \times L_{int}(\lambda, T_b) + (1 - F) \times L_{int}(\lambda, T_D) \right]$$

$$\approx \frac{2\pi c q (EQE)}{\lambda^4} \left[F \exp\left({-hc}/{\lambda k T_b} \right) + (1 - F) \exp\left({-hc}/{\lambda k T_D} \right) \right]. \tag{3}$$

The net background current density is finally obtained by integrating the differential contribution over all incident wavelengths:

$$J_b(T_b, T_D) = \int_{\lambda_1}^{\lambda_2} L_J(\lambda, T_b, T_D)\, d\lambda . \tag{4}$$

Having measured the present device's EQE spectra at a series of operating temperatures (T_D), we can perform this integral for any assumed background temperature (T_b) by summing over the fine mesh of wavelengths provided by the FTIR (resolution ≈ 1 nm). We can also determine how much of J_b is due to photoexcitation within the resonance linewidth *vs.* how much is parasitic photocurrent generated at wavelengths outside this band. Combining with the measured *J-V* characteristics, we can then use Eq. (1) to determine $D^*(T_b, T_D)$ at the series of RCID operating temperatures for which EQE data are available.

We will compare with the corresponding D^* expected for a state-of-the-art HgCdTe detector operating at the same T_D, assuming EQE = 85% at all wavelengths and dark current given by Rule '07 when the cut-off wavelength is 5 μm. In both cases, we integrate Eq. (4) over the entire MWIR spectral band ($\lambda_1 = 3$ μm, $\lambda_2 = 5$ μm). To simulate a realistic system scenario, we assume that the detector is housed in a dewar with cold shielding, such that most incident angles view a background at the detector operating temperature of T_D. Only the input optic exposes the detector to background radiation at the scene temperature T_s, which is assumed to be 300 K. In particular, we will consider an f/4 optic, for which only $F \approx 0.6\%$ of the background is at T_s while 99.4% is at T_D.

Figure 12 plots the ratio of background photocurrent, as derived from Eq. (4), to total noise current corresponding to all three contributions in the denominator of Eq. (1). This ratio is plotted as a function of temperature for the broadband device (red points) and an RCID with the characteristics shown in Figs. 5-11 (blue points). The background photocurrent is relatively unimportant at higher temperatures where the dark current in both devices is large. However, J_d decreases by orders of magnitude with decreasing temperature, so the background photocurrent from the scene comes to dominate even though the f/4 optic exposes only the small fraction F of the field of view to the scene. The temperature at which this crossover occurs varies considerably with device type, and whether the f/4 optic is employed (filled points) or the entire field of view ($F = 1$) is exposed to background at the scene temperature (no optic, open points). Because the RCID strongly suppresses background irradiation outside the narrow resonance bandwidth, its background photocurrent doesn't become dominant until a lower T_D. When the detector's entire field of view observes the background, the associated noise naturally becomes dominant sooner (at a higher temperature). It follows that the RCID's strong suppression of background noise is even more advantageous in that case. In the opposite limit of an optic with larger f/#, for which a smaller angular fraction of the input is exposed to the scene background, the cross-over to background-dominance shifts to lower temperature.

In Fig. 13, D^* *vs.* detector operating temperature from Eq. (1), assuming the f/4 optic, for the broadband HgCdTe device (red points) is compared to that of the RCID (blue points). D^* for the RCID is lower at $T_D \geq 200$ K due to its higher (non-optimized) dark current. In this limit the RCID's substantial suppression of background photocurrent does not play a significant role.

However, we saw in Fig. 12 that with decreasing temperature the background photocurrent eventually comes to dominate (*e.g.*, by orders of magnitude in the broadband device at $T_D <$ 150 K). At that point D^* no longer increases with decreasing T_D. But since background current is strongly suppressed in the RCID, its D^* continues to increase to lower T_D below 150 K. Only at 125 K does the scene background become strong enough that D^* no longer increases. In fact, it decreases at $T_D = 100$ K due to the rapid fall-off of peak EQE seen in Figure 11. Nonetheless, despite the RCID's much lower EQE peaks of 43% at 150 K, 33% at 125 K, and 23% at 100 K, D^* for the RCID exceeds that of the broadband device at all $T_D \leq 150$ K for which the RCID was characterized. At 125 K, the estimated D^* of $\approx 5.5 \times 10^{12}$ cm Hz^{½}/W is 3.3× higher.

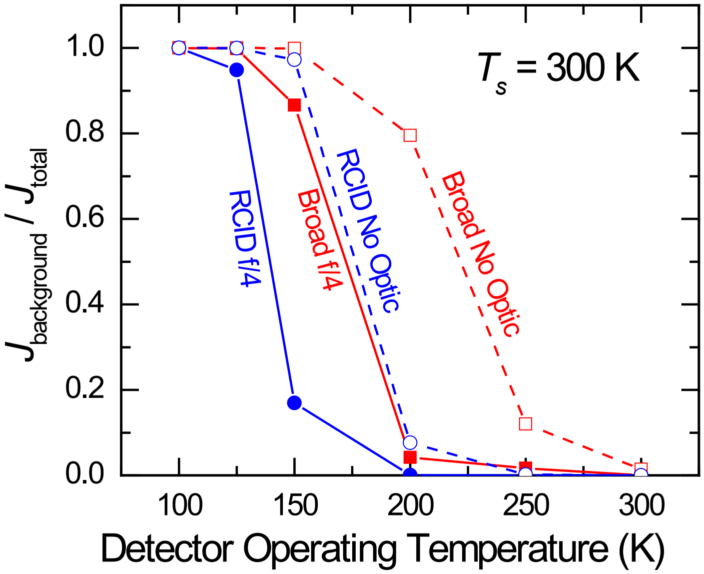

Figure 12 – Ratio of background photocurrent to total noise current for a state-of-the-art broadband HgCdTe device *vs*. an RCID with the EQE(λ,T_D) and J_d(T_D) characteristics shown in Figs. 5-11 (blue points). The filled points assume an f/4 optic that exposes only $F \approx 0.6\%$ of the field of view to background at the scene temperature, whereas the open points assume the entire field of view observes background at T_s ($F = 1$, no optic).

We saw in Fig. 12 that the RCID's delay of background dominance becomes more pronounced when a larger fraction of the field of view observes the background (smaller f/# or no optic). The RCID's D^* will then become higher at a higher T_D, and by a larger maximum factor with decreasing temperature. Of course, the details of this analysis change if the scene is hotter or colder than 300 K. We also note that for both devices in this system scenario, the cold-shielded background at T_D never plays a significant role.

Although it would be beneficial in such scenarios to insert a narrow-bandpass filter into the broadband detector's field of view, the filter itself may contribute substantial background unless it is cooled. For this reason cold filters, and even cold filter wheels, are sometimes employed in conjunction with broadband detectors and imagers [24]. However, for MWIR wavelengths beyond 4.5 μm the minimum bandwidth for such a filter is typically at least ≈ 100 nm [25]. Thus besides introducing 10-20% transmission loss, the background current generated near the wavelength of interest is 5× higher than for an RCID with $\delta\lambda \approx 20$ nm (and narrower RCID linewidths are anticipated in the future). For applications requiring rapid tuning of the central wavelength, a mechanical cold filter wheel will be much slower and less flexible than an RCID with MEMS or piezoelectric dynamic tuning capability that will be discussed briefly in Section 7 below.

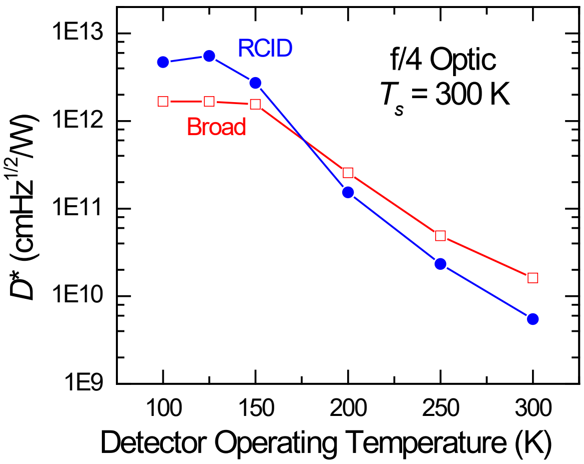

Figure 13 – Specific detectivity *vs.* detector operating temperature T_D for the scenario with an f/4 optic. The RCID performance (blue points), based on the measured dark currents and EQE spectra at each temperature shown in Figs. 5-11, is compared to that for the state-of-the-art broadband HgCdTe device (red points).

The RCID's higher D^* at low temperatures depends critically on its strong suppression of the scene background at non-resonant wavelengths. While the background flux density at 300 K increases substantially with increasing wavelength, the contribution to J_b from $\lambda > \lambda_{\text{res}} + 3\delta\lambda$ is only ≈ 1% of the total because EQE(λ) is quite small in that region as we see in Figure 9. The shorter-wavelength range $\lambda < \lambda_{\text{res}} - 3\delta\lambda$ contributes 24% of the total J_b, while the remaining 75% is due to background near the resonance ($\lambda_{\text{res}} - 3\delta\lambda < \lambda < \lambda_{res} + 3\lambda$). Despite the RCID's higher EQE at $\lambda < 3.5$ µm, black body emission is weak in that range so the shorter-wavelength contribution comes mostly from wavelengths in the 4.2-4.5 µm range where the shoulder of the EQE's resonance peak is somewhat softer. It will be especially beneficial if future designs with higher cavity Q can produce a narrower $\delta\lambda$ and even smaller off-resonance EQE(λ).

It was noted in the Introduction that some of the previous RCID demonstrations have produced similar EQEs, $\delta\lambda$ almost as narrow, and slightly higher D^* relative to Rule '07 when background currents are ignored. For example, $\Gamma_{\text{D}^*} \approx 0.48$ and $\delta\lambda = 25$ nm for $\lambda_{res} = 3.7$ µm at 200 K in Ref. [16], and $\Gamma_{\text{D}^*} \approx 0.46$ and $\delta\lambda \approx 50$ nm for $\lambda_{res} = 4.4$ µm at 300 K (TE polarization) in Ref. [18], as compared to $\Gamma_{\text{D}^*} \approx 0.32$ and $\delta\lambda = 19$ nm for $\lambda_{res} = 4.6$ µm at 150 K with the present device. However, all of the non-resonant EQEs reported for earlier devices were much larger than those illustrated in Figure 9. The resonance shoulders have typically been at the 5-10% level at shorter wavelengths and ≥ 3% at longer wavelengths, or much higher, as compared to ≈ 1% and < 0.5%, respectively, for the present RCID. Although for those devices we do not have the detailed data required to repeat the D^* analysis discussed above, it appears their noise photocurrents induced by the scene background at non-resonance wavelengths would have much greater effect on the resulting D^*.

E.5 *nBn* performance simulation

To investigate the future prospects for increasing the quantum efficiency and reducing the dark current, we have simulated various aspects of the RCID performance. This was done using

NRL MULTIBANDS$^{\text{TM}}$ [26], a software package that was co-developed by some of the present authors and is based on physical concepts and mathematical formalisms described in Ref. [27].

Figure 14 illustrates the calculated conduction (blue) and valence (red) band profiles, and respective Fermi levels (dashed curves), for the present *nBn* detector structure at 300 K under -150 mV bias.

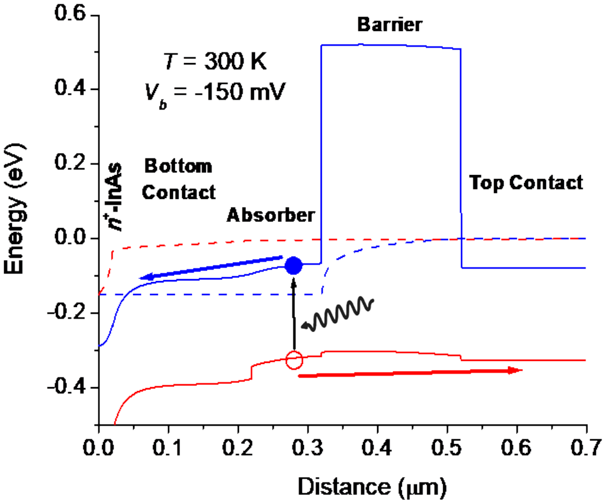

Figure 14 – Simulated conduction (blue) and valence (red) band profiles in the *nBn* detector structure at 300 K when operated at -150 mV bias. The respective Fermi levels are shown as dashed curves.

Figure 15 plots the corresponding profiles for electron (blue) and hole (red) carrier concentrations in the structure without illumination. The smooth variation for holes is consistent with unimpeded collection of the minority carriers, whereas the barrier clearly blocks electron transport from the top contact. The applied field depletes electrons from the absorber region closest to the barrier. However, spillover from the doped bottom contact layer increases the density at the opposite end of the absorber, to a value much higher than would normally be present in an isolated unintentionally-doped InAs/InAsSb superlattice. Similarly, spillover from the heavily-doped n^+-InAs capping layer increases the electron concentration in the adjacent region of the bottom contact.

The Auger decay rate r_{Aug} corresponding to the carrier concentrations at a given position is:

$$r_{Aug} = (C_n n + C_p p)(np - n_0 p_0)\ . \qquad (5)$$

Here C_n and C_p are the Auger coefficients for events involving two electrons and one hole *vs.* those involving two holes and one electron, respectively, while n_0 and p_0 are the electron and hole populations in thermal equilibrium. Since the hole concentration is quite small everywhere in the present structure, we can ignore the term proportional to C_p. By fitting the observed dark current density in test detector structures with the same absorber, assuming a Shockley-Read-Hall (SRH) lifetime of 1 μs in the absorber, and using the wavelength dependence for C_n in Ref. [28], C_n is ≈ 5×10^{-27} cm^6/s in the wider-gap bottom contact layer and ≈ 8×10^{-27} cm^6/s in the absorber layer at 300 K. These values are about an order of magnitude larger than in type-II InAs/Ga(In)Sb superlattices with the same energy gaps, which is consistent with the available literature [29,30]. The alternative assumption that the lifetime is dominated by SRH recombination requires an unrealistically short lifetime of a few 10's of ns.

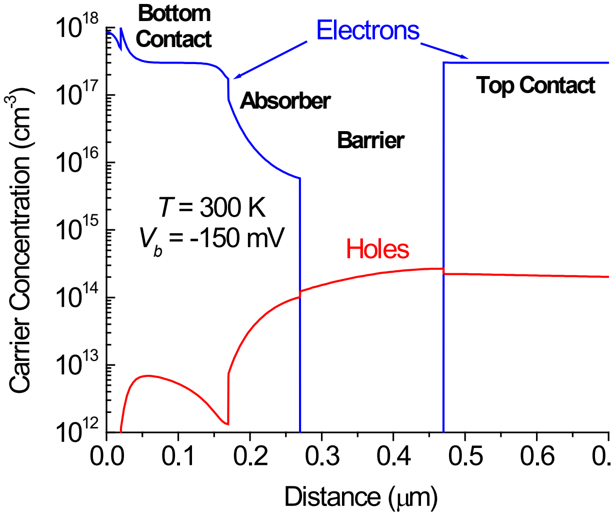

Figure 15 – Simulated electron (blue) and hole (red) concentrations *vs*. position in the *nBn* detector structure of Fig. 14 without illumination.

Figure 16 plots the resulting spatial profile of the Auger recombination rate. Electrons and holes recombine in the top contact layer (blue portion of the curve), where $np - n_0p_0 > 0$ because holes are collected and the electrons cannot escape. However, $np - n_0p_0 < 0$ in the absorber and bottom contact layers (red portions of the curve), where the applied field depletes carriers and $p << p_0$ even though $n > n_0$ at some positions. The resulting negative Auger rate corresponds to impact ionization, which dominates the thermal generation of additional electron-hole pairs in the present structure at temperatures near ambient.

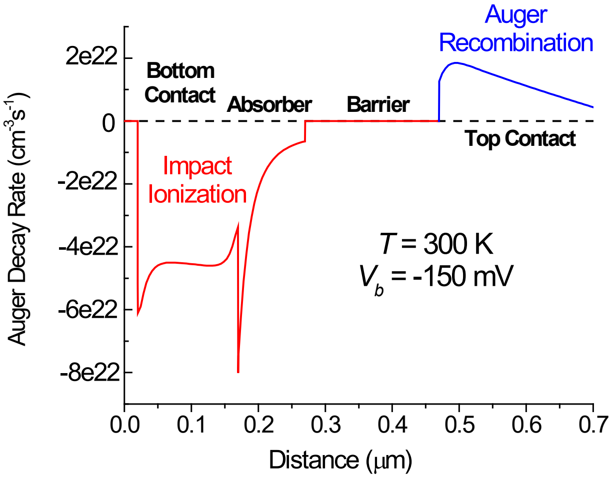

Figure 16 – Simulated profile of the Auger recombination rate in the *nBn* detector structure of Figure 14. A negative Auger rate (red portion of the curve) corresponds to impact ionization that generates additional electron-hole pairs.

The simulation projects that for room temperature operation, there is no appreciable advantage to reducing the thickness of the absorber. However, lower doping of the bottom contact layer may potentially reduce the dark current due to impact ionization. Analogous simulations find that at lower temperatures, the dark current is dominated by inverse SRH processes, assuming the Auger coefficient remains the same. In that limit, it may be possible to reduce the dark current by reducing the absorber thickness.

The experimental EQE of 58% (from the FTIR characterization) at 300 K is already relatively favorable. Nonetheless, further improvement may be possible by increasing the reflectivity of the top mirror and minimizing parasitic absorption in the top contact layer. At lower temperatures, the rapid decline of the peak EQE in Fig. 11 is attributable primarily to the shift of absorber cut-off wavelength relative to the resonance wavelength (see Fig. 3). Future designs intended for low-temperature operation can compensate by employing a longer cut-off and/or increasing the cavity *Q*.

E.6 Frequency Response

Another significant advantage of the RCID over a conventional broadband IR detector is its potential for much higher frequency response. Because the RCID's absorber is ≈ 50 times thinner, photoexcited minority carriers can be extracted much more rapidly. Because the response is then limited by the RC time constant, a small mesa diameter that minimizes the capacitance is advantageous.

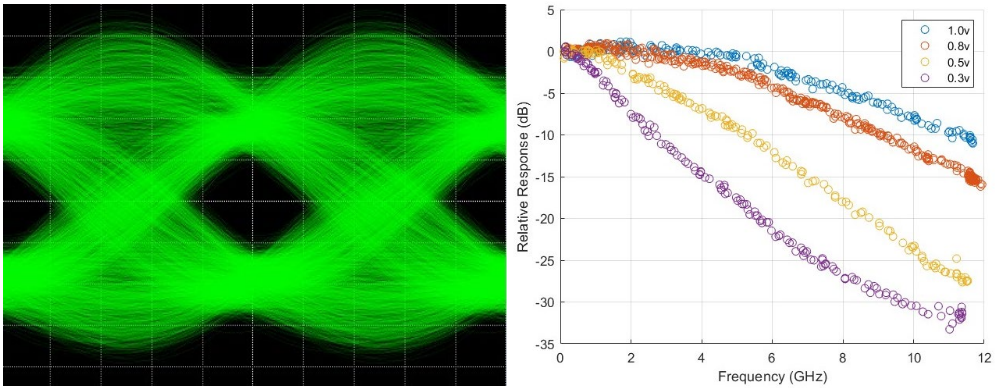

Figure 17 – High-speed measurements performed at Intraband on an RCID with 25 μm diameter: (a) Eye diagram for 5 Gb/s data rate; (b) Relative frequency response at bias voltages of 0.3, 0.5, 0.8, and 1.0 V [32].

Intraband and Praevium have collaborated with NRL on an Army STTR program (managed by Dr. Michael Gerhold) to develop an MWIR free space optical communication system that combines a fast QCL source with a fast RCID receiver [22]. For this effort, Intraband used an rf probe to characterize the frequency response of an RCID with 25-μm diameter, which was grown by NRL and processed by Praevium. Using a calibrated QCL, Intraband determined the peak EQE to be 52%. Intraband also used an rf probe to perform high-frequency measurements. Figure 17(a) illustrates the eye diagram at 5 Gb/s data rate, for which the bit-error-ratio (BER) at T = 20 °C was < 10^{-7} [32]. Figure 17(b) illustrates the relative response *vs.* frequency at a series of bias voltages [32]. At a bias of 1 V, the -3dB response is 7 GHz. However, whereas the RCIDs tested to date provide high peak EQE at a low bias voltage of only 150 mV, a larger bias is apparently required to sweep the photoexcited carriers out of the absorber rapidly enough for high frequency response.

E.7 References:

1. J. R. Meyer, I. Vurgaftman, C. L. Canedy, W. W. Bewley, C. S. Kim, C. D. Merritt, M. V. Warren, and M. Kim, “Resonant-Cavity Infrared Photodetectors with Fully-Depleted Absorbers,” U.S. Patent #10,062,794, 28 August 2018.
2. M. S. Ünlü and S. Strite, “Resonant cavity enhanced photonic devices,” *J. Appl. Phys.* **78**, 607-639 (1995).
3. M. Guan and C. Chang-Hasnain, “Resonant-cavity-enhanced p-i-n photodetector using a high-contrast-grating for 940nm,” *Opt. Expr.* **30**, 9298-9306 (2022).
4. A. M. Green, D. G. Gevaux, C. Roberts, P. N Stavrinou, and C. C. Phillips, “$\lambda \approx 3$ μm InAs resonant-cavity-enhanced photodetector,” *Semicond. Sci. Technol.* **18**, 964-967 (2003).
5. M. Böberl, T. Fromherz, T. Schwarzl, G. Springholz, and W. Heiss, “IV–VI resonant-cavity enhanced photodetectors for the mid-infrared,” *Semicond. Sci. Technol.* **19**, L115-L117 (2004).
6. M. Arnold, D. Zimin, and H. Zogg, “Resonant-cavity-enhanced photodetectors for the mid-infrared,” *Appl. Phys. Lett.* **87**, 141103 (2005).
7. J. Wang, J. Hu, P. Becla, A. M. Agarwal, and L. C. Kimerling, “Resonant-cavity-enhanced mid-infrared photodetector on a silicon platform,” *Opt. Expr.* **18**, 12890-12896 (2010).
8. F. Felder, M. Arnold, M. Rahim, C. Ebneter, and H. Zogg, “Tunable lead-chalcogenide on Si resonant cavity enhanced midinfrared detector,” *Appl. Phys. Lett.* **91**, 101102 (2007).
9. N. Quack, S. Blunier, J. Dual, F. Felder, M. Arnold, and H. Zogg, “Mid-infrared tunable resonant cavity enhanced detectors”, *Sensors* **8**, 5466-5478 (2008).
10. W. E. Tennant, “”Rule 07” revisited: Still a good heuristic predictor of *p/n* HgCdTe photodiode performance?”, *J. Electron. Mater.* **39**, 1030-1035 (2010).
11. T. A. O’Loughlin, G. R. Savich, D. E. Sidor, B. T. Marozas, T. D. Golding, K. D. Jamison, L. Fredin, B. Fowler, W. Priyantha, and G. W. Wicks, “Mid-IR resonant cavity detectors”, *J. Vac. Sci. Technol. B* **35**, 02B111 (2017).
12. C. L. Canedy, W. W. Bewley, C. D. Merritt, C. S. Kim, M. Kim, M. V. Warren, E. M. Jackson, J. A. Nolde, C. A. Affouda, E. H. Aifer, I. Vurgaftman, and J. R. Meyer, “Resonant-cavity infrared detector with five-quantum-well absorber and 34% external quantum efficiency at 4 μm,” *Opt. Expr.* **27**, 3771-3781 (2019).
13. A. P. Craig, F. Al-Saymari, M. Jain, A. Bainbridge, G. R. Savich, T. Golding, A. Krier, G. W. Wicks, and A. R. Marshall, “ Resonant cavity enhanced photodiodes on GaSb or the mid-wave infrared,” *Appl. Phys. Lett.* **114**, 151107 (2019).
14. V. Letka, A. Bainbridge, A. P. Craig, F. Al-Saymari, and A. R. J. Marshall, “Resonant cavity-enhanced photodetector incorporating a type-II superlattice to extend MWIR sensitivity,” *Opt. Expr.* **27**, 23970-23980 (2019).
15. V. Letka, A. P. Craig, A. Bainbridge, and A. R. J. Marshall, “A superlattice-based resonant cavity-enhanced photodetector operating in the long-wavelength infrared,” *Appl. Phys. Lett.* **117**, 073503 (2020).
16. A. Bainbridge, A. P. Craig, F. Al-Saymari, A. Krier, and A. R. J. Marshall, “Resonant Cavity–Enhanced Photodiodes for Spectroscopy of C─H Bonds,” *phys. stat. sol. (a)* **218**, 2100056 (2021).

17. A. Bainbridge, L. A. Hanks, A. P. Craig, and A. R. J. Marshall, "Resonant cavity-enhanced photodiode array for miniaturised spectroscopic sensing," *Opt. Expr.* **30**, 3230-3237 (2022).
18. A. Kamboj, L. Nordin, A. J. Muhowski, D. Woolf, and D. Wasserman, "Room-Temperature Mid-Wave Infrared Guided-Mode Resonance Detectors," *IEEE Phot. Tech. Lett.* **34**, 615-618 (2022).
19. P. Petluru, A. J. Muhowski, A. Kamboj, N. C. Mansfield, M. Bergthold, E. A. Shaner, J. F. Klem, and D. Wasserman, "All-epitaxial resonant cavity enhanced long-wave infrared detectors for focal plane arrays," *Appl. Phys. Lett.* **122**, 021101 (2023).
20. C. L. Canedy, C. S. Kim, M. Kim, D. C. Larrabee, J. A. Nolde, W. W. Bewley, I. Vurgaftman, and J. R. Meyer, "High-Power, Narrow-Ridge, Mid-Infrared Interband Cascade Lasers," *J. Vac. Sci. Technol. B* **26**, 1160-1162 (2008).
21. J. A. Nolde, E. M. Jackson, M. F. Bennett, C. A. Affouda, E. R. Cleveland, C. L. Canedy, I. Vurgaftman, G. G. Jernigan, J. R. Meyer, E. H. Aifer, "Reticulated Shallow Etch Mesa Isolation (RSEMI) for Controlling Surface Leakage in GaSb-Based Infrared Detectors," *Appl. Phys. Lett.* **111**, 051102 (2017).
22. M. Turville-Heitz, J. Ryu, J. D. Kirch, S. Jacobs, R. Marsland, T. Earles, S. Ruder, K. Oresick, D. Botez, and L. J. Mawst, "High-Power Mid-Infrared Quantum Cascade Lasers for Free-Space Communications," *Proc. IEEE Photonics Conf.* (13-17 November 2022, Vancouver Canada).
23. R. W. Boyd, "Radiometry and the Detection of Optical Radiation," (Wiley, 1983); spectralcalc.com/blackbody.
24. N. Gat, J. Zhang, M. D. Li, L. Chen, and H. Gurrola, "Variable Cold Stop for Matching IR Cameras to Multiple f-number Optics," *Proc. SPIE* **6542**, 654215 (2007).
25. edmundoptics.com/p/467m-cwl-250mm-diameter-015-fwhm-ir-bandpass-filter/27182/; thorlabs.com/thorproduct.cfm?partnumber=FB5068-100.
26. M. P. Lumb, I. Vurgaftman, C. A. Affouda, J. R. Meyer, E. H. Aifer and R. J. Walters, "Quantum Wells and Superlattices for III-V Photovoltaics and Photodetectors," *Proc. SPIE* 8471, 84710A (2012).
27. I. Vurgaftman, M. P. Lumb, and J. R. Meyer, *Bands and Photons in III-V Semiconductor Quantum Structures* (Oxford University Press, 2021).
28. J. R. Meyer, C. L. Canedy, M. Kim, C. S. Kim, C. D. Merritt, W. W. Bewley, and I. Vurgaftman, "Comparison of Auger Coefficients in Type I and Type II Quantum Well Midwave Infrared Lasers," *IEEE J. Quant. Electron.* **57**, 2500110 (2021).
29. L. Höglund, D. Z. Ting, A. Soibel, A. Fisher, A. Khoshakhlagh, C. J. Hill, S. Keo, and S. D. Gunapala, "Minority carrier lifetime in mid-wavelength infrared InAs/InAsSb superlattices: Photon recycling and the role of radiative and Shockley-Read-Hall recombination mechanisms," *Appl. Phys. Lett.* **105**, 193510 (2014).
30. R. E. DeWames, J. Schuster, E. A. DeCuir Jr., N. K. Dhar, "Recombination Processes in InAs/InAsSb Type II Strained Layer Superlattice MWIR nBn Detectors," *Proc. SPIE* **11002**, 110020W (2019).
31. V. Jayaraman, B. Kolasa, C. Lindblad, A. Cazabat, C. Burgner, S. Segal, K. Lascola, F. Towner, and F. Xie, *Proc. SPIE* **11300**, 113000M (2020), "Tunable room-temperature continuous-wave mid-infrared VCSELs."
32. R. Marsland, M. Turville-Heitz, J.-H. Ryu, C. L. Canedy, I. Vurgaftman, V. Jayaraman, T. Earles, S. Ruder, B. Knipfer, J.R. Meyer, D. Botez, and L.J. Mawst, SPIE Phot. West (27 January - 1 February 2024, San Francisco CA), "Room-temperature, directly modulated DFB-QCLs and resonant-cavity infrared detectors (RCIDs) for 5 Gb/s OOK free-space, mid-wave infrared atmospheric laser communication."

F. Impact & Transitions

The success of the RCID development under this program directly contributed to:

(1) An ONR D&I New Start entitled "Mid-Wave Infrared Detectors with Tunable Narrow-Band Spectral Response" (FY24-26, $300 K per year)

(2) An ONR D&I New Start entitled "Resonant Cavity Infrared Detectors (RCIDs) for MWIR Polarimetric Sensing" (FY24, $200 K, with hopes for extension)

(3) A parallel Navy SBIR Topic: "Mid-Wave Infrared Detectors with Tunable Narrow-Band Spectral Response", which (2) will support. Four Phase I contracts were recently awarded

(4) An NRL FY25 6.2 New Start Proposal entitled "Sensitive Detection of LWIR Laser Signals" (RAC decision soon)

(5) Joint Navy STTR (with Intraband and Praevium) to develop an LWIR free space optical communication system that combines fast LWIR QCLs with fast LWIR RCIDs - Currently in Phase II.

(6) Invitation for presentation of an RCID-related virtual seminar to Shipboard Panoramic Electro-Optic/Infrared (SPEIR)

(7) Invited presentation at Photonics West

(8) Demonstration with Princeton University of N_2O sensing with combination of narrow-band MWIR RCID with broadband interband cascade LED source. An Material Transfer Agreement (MTA) is currently being negotiated to provide Princeton with additional RCIDs at more favorable wavelengths.

(9) Spin-off proposal (with Chip Design Systems & Praevium) of resonant cavity LEDs for IR Scene Projection

Praevium is currently considering licensing of the NRL patents for RCID commercialization

G. Publications

G.1 Refereed Journal Articles

1. J. R. Meyer, C. S. Kim, M. Kim, C. L. Canedy, C. D. Merritt, W. W. Bewley, and I. Vurgaftman, Sensors 21, 599 (2021), "Interband Cascade Photonic Integrated Circuits on Native III-V Chip."
2. C. L. Canedy, E. M. Jackson, R. L. Espinola, M. R. Pauli, J. M. Auxier, C. S. Kim, M. Kim, J. A. Nolde, E. H. Aifer, I. Vurgaftman, V. Jayaraman, B. Kolasa, R. Marsland, B. Knipfer, and J. R. Meyer, Opt. Expr. 31, 35225 (2023), "Midwave Infrared Resonant Cavity Infrared Detectors (RCIDs) with Suppressed Background Noise."

G.2 Patents

1. J. R. Meyer, I. Vurgaftman, C. L. Canedy, W. W. Bewley, C. S. Kim, C. D. Merritt, M. V. Warren, and M. Kim, U.S. Patent #10,559,704, 11 February 2020, "In-Plane Resonant-Cavity Infrared Photodetectors with Fully-Depleted Absorbers."
2. J. R. Meyer, I. Vurgaftman, C. L. Canedy, W. W. Bewley, C. S. Kim, C. D. Merritt, M. V. Warren, R. J. Weiblen, and M. Kim, U.S. Patent #11,125,689, 21 September 2021, "Highly Stable Semiconductor Laser for III-V and Silicon Photonic Integrated Circuits."

3. J. R. Meyer, I. Vurgaftman, C. L. Canedy, W. W. Bewley, C. S. Kim, C. D. Merritt, M. V. Warren, R. J. Weiblen, and M. Kim, U. S. Patent #11,619,583, 4 April 2023, "Highly Stable Semiconductor Laser for III-V and Silicon Photonic Integrated Circuits."
4. J. R. Meyer, I. Vurgaftman, C. L. Canedy, W. W. Bewley, C. S. Kim, C. D. Merritt, M. V. Warren, R. J. Weiblen, and M. Kim, U.S. Patent #11,719,633, 8 August 2023, "Highly Stable Semiconductor Laser for III-V and Silicon Photonic Integrated Circuits."

G.3 Conference Proceedings Papers

1. N. P. Li, L. Tao, J. McSpiritt, E. M. Jackson, C. L. Canedy, C. D. Merritt, M. Kim, C. S. Kim, W. W. Bewley, J. A. Nolde, E. H. Aifer, I. Vurgaftman, J. R. Meyer, and M. A. Zondlo, Proc. SPIE 12516, 1251623 (2023), "Resonant Cavity Infrared Detectors for Scalable Gas Sensing."

G.4 Invited Conference Presentations

1. J. R. Meyer, M. Kim, C. S. Kim, C. L. Canedy, C. D. Merritt, W. W. Bewley, and I. Vurgaftman, IEEE Photonics Society Summer Topical on Silicon Integrated Mid-Infrared Photonics (19-21 July 2021, Cabos San Lucas Mexico, Virtual), "Mid-IR Photonic Integrated Circuits."
2. J. R. Meyer, C. S. Kim, M. Kim, C. L. Canedy, C. D. Merritt, W. W. Bewley, S. Tomasulo, E. M. Jackson, J. A. Nolde, E. H. Aifer, and I. Vurgaftman, NRL-NRO FPA Consortium Meeting (2 November 2021, NRL), "Resonant Cavity Infrared Detectors (RCIDs)."
3. J. R. Meyer, C. S. Kim, M. Kim, C. L. Canedy, W. W. Bewley, A. Grede, C. D. Merritt, and I. Vurgaftman, Advanced Technology for National Security Conference (1-2 March 2022, Lexington MA), "Next-Generation Lasers, Resonant Cavity Detectors, & Photonic Integrated Circuits for MWIR & LWIR Optical Sensing."
4. C. S. Kim, M. Kim, A. Grede, C. L. Canedy, C. D. Merritt, W. W. Bewley, S. Tomasulo, I. Vurgaftman, and J. R. Meyer, Compound Semiconductor Week (1-3 June 2022, Ann Arbor MI), "Recent Advances of Interband Cascade Lasers and Resonant Cavity Infrared Detectors."
5. V. Jayaraman, B. Kolasa, C. Burgner R. Marsland, B. Knipfer, M. Turville-Heitz, J. Ryu, L. J. Mawst, D. Botez, C. L. Canedy, E. M. Jackson, R. L. Espinola, C. S. Kim, E. H. Aifer, I. Vurgaftman, and J.R. Meyer, Int. Conf. Quantum Engineered Sensing & Information Technology (27-30 June 2023, Paris France), "Detectors and Emitters for Mid-Infrared Optical Communications."
6. C. S. Kim, M. Kim, C. L. Canedy, E. M. Jackson, R. L. Espinola, J. A. Nolde, E. H. Aifer, I. Vurgaftman, J.R. Meyer, V. Jayaraman, B. Kolasa, C. Burgner, B. Knipfer, and R. Marsland, SPIE Phot. West (27 January - 1 February 2024, San Francisco CA), "High-Sensitivity Mid-Wave Resonant Cavity Infrared Detectors."

G.5 Contributed Conference Presentations

1. N. P. Li, L. Tao, J. McSpiritt, M. A. Zondlo, E. M. Jackson, M. Kim, C. S. Kim, C. L. Canedy, C. D. Merritt, W. W. Bewley, J. A. Nolde, E. H. Aifer, I.

Vurgaftman, and J. R. Meyer, Laser Applications to Chemical, Security and Environmental Analysis, (11-15 July 2022, Vancouver Canada), "Room temperature detection of N2O using a resonant cavity mid-IR detector and interband cascade LED."

2. N. P. Li, L. Tao, J. McSpiritt, M. A. Zondlo, E. M. Jackson, C. L. Canedy, C. D. Merritt, M. Kim, C. S. Kim, W. W. Bewley, J. A. Nolde, E. H. Aifer, I. Vurgaftman, and J. R. Meyer, Field Laser Applications in Industry and Research (12-16 September 2022, Aix-les-Bains France), "Towards Low-cost Optical Gas Sensors: Demonstration of Chip-scale Detection of N2O by Combining an Interband Cascade LED with Resonant Cavity Infrared Detector."
3. N. P. Li, L. Tao, J. McSpiritt, E. M. Jackson, C. L. Canedy, C. D. Merritt, M. Kim, C. S. Kim, W. W. Bewley, J. A. Nolde, E. H. Aifer, I. Vurgaftman, J. R. Meyer, and M. A. Zondlo, SPIE Defense and Commercial Sensing (30 April – 4 May 2023, Orlando FL), "Resonant Cavity Infrared Detectors for Scalable Gas Sensing."
4. C. L. Canedy, E. M. Jackson, R. L. Espinola, C. S. Kim, E. H. Aifer, I. Vurgaftman, V. Jayaraman, B. Kolasa, R. Marsland, B. Knipfer, M. Turville-Heitz, J. Ryu, L. J. Mawst, D. Botez, and J. R. Meyer, 16th Int. Conf. Mid-Infrared Optoelectronic Materials and Devices (6-10 August 2023, Norman OK), "MWIR Resonant Cavity Infrared Detectors (RCIDs) with High Quantum Efficiency and High Frequency Response."
5. R. Marsland, M. Turville-Heitz, J.-H. Ryu, C. L. Canedy, I. Vurgaftman, V. Jayaraman, T. Earles, S. Ruder, B. Knipfer, J.R. Meyer, D. Botez, and L.J. Mawst, SPIE Phot. West (27 January - 1 February 2024, San Francisco CA), "Room-temperature, directly modulated DFB-QCLs and resonant-cavity infrared detectors (RCIDs) for 5 Gb/s OOK free-space, mid-wave infrared atmospheric laser communication."